Living myofibroblast–silicon composites for probing electrical coupling in cardiac systems

Menahem Y. Rotenberg[a,1], Naomi Yamamoto[b], Erik N. Schaumann[b], Laura Matino[c,d], Francesca Santoro[c], and Bozhi Tian[a,b,e,1]

[a]The James Franck Institute, The University of Chicago, Chicago, IL 60637; [b]Department of Chemistry, The University of Chicago, Chicago, IL 60637; [c]Tissue Electronics, Center for Advanced Biomaterials for Healthcare, Istituto Italiano di Tecnologia, 80125 Naples, Italy; [d]Department of Chemical Materials and Industrial Production Engineering, University of Naples Federico II, 80125 Naples, Italy; and [e]The Institute for Biophysical Dynamics, The University of Chicago, Chicago, IL 60637

Edited by John A. Rogers, Northwestern University, Evanston, IL, and approved September 26, 2019 (received for review August 8, 2019)

Traditional bioelectronics, primarily comprised of nonliving synthetic materials, lack cellular behaviors such as adaptability and motility. This shortcoming results in mechanically invasive devices and nonnatural signal transduction across cells and tissues. Moreover, resolving heterocellular electrical communication in vivo is extremely limited due to the invasiveness of traditional interconnected electrical probes. In this paper, we present a cell–silicon hybrid that integrates native cellular behavior (e.g., gap junction formation and biosignal processing) with nongenetically enabled photosensitivity. This hybrid configuration allows interconnect-free cellular modulation with subcellular spatial resolution for bioelectric studies. Specifically, we hybridize cardiac myofibroblasts with silicon nanowires and use these engineered hybrids to synchronize the electrical activity of cardiomyocytes, studying heterocellular bioelectric coupling in vitro. Thereafter, we inject the engineered myofibroblasts into heart tissues and show their ability to seamlessly integrate into contractile tissues in vivo. Finally, we apply local photostimulation with high cell specificity to tackle a long-standing debate regarding the existence of myofibroblast–cardiomyocyte electrical coupling in vivo.

optical stimulation | cardiomyocytes | myofibroblast | silicon nanowires | electrical coupling

Electronic and optoelectronic systems for in vivo cellular interrogation require minimally invasive tissue access within the 3-dimensional tissue volume. Micropipette electrodes (1, 2), microelectrode arrays (3, 4), and field effect transistors (5–7) have enabled numerous single-cell studies, although they are typically substrate-bound devices. Optogenetics can offer mechanistic insights into cellular processes, but it requires genetic modification (8–10), which limits its potential clinical applications. Recent developments in flexible implantable devices have yielded biointerfaces (11–15) that are minimally invasive and can integrate wireless electronics and optoelectronics with optogenetics. Currently, the material tool kit is primarily based on synthetic components. When interfacing with live and dynamically changing tissues, seamless integration of the device is limited by the remaining mechanical invasiveness of the materials and nonnatural biological signal transduction at the biointerfaces. We propose that living hybrid systems with dynamic and developing behaviors can offer new opportunities for bioelectric interfaces due to the adaptability and motility of the cellular components and the diverse physical properties of the materials components.

Silicon nanowires (SiNWs) can be spontaneously internalized by many cell types (16), which allows for hybridization while avoiding abrasive electroporation, sonication, or genetic modification. Following internalization, cell–SiNW hybrids may be harvested using standard cell culture techniques for both in vitro and in vivo downstream applications (Fig. 1*A*). The light scattering from SiNWs distinguishes the hybrids from surrounding SiNW-free cells, eliminating the need for fluorescent labeling. Using a focusing laser, the cell–SiNWs hybrids may be photostimulated via photoelectric (17) and photothermal (18) mechanisms. As the photostimulation depends on the colocalization of light and the SiNW, a localized stimulus can be applied deep into the tissue. Moreover, their freestanding nature minimizes their invasiveness due to persistent in vivo mechanical mismatch.

In this work, we apply our cell–SiNW hybrid system to the investigation of intracellular electrical coupling in cardiac systems. Hybridizing SiNWs with myofibroblasts (MFs), we demonstrate that this living hybrid tool can be used for investigating intercellular electrical coupling in vitro and in vivo. Using the MF–SiNW hybrid tool to compare MF–MF electrical coupling with MF–cardiomyocytes (CMs) coupling in vitro, we detect 2 different calcium flux propagation mechanisms—one for amplified CM propagation and the other for passive MF propagation. We report that, unlike bare SiNWs, our MF–SiNW hybrids can be seamlessly integrated into contractile cardiac tissue. Finally, we use our living hybrid tool to tackle the long-standing debate regarding the existence of in vivo MF–CM heterocellular coupling.

In Vitro Electric Coupling and Optical Pacing

Coaxial SiNWs were synthesized as previously reported (17, 19). Scanning electron microscope (SEM) images of the SiNWs show a 1-dimensional geometry with a ∼300-nm diameter and a core-shell

Significance

Techniques for intracellular electrical interrogation are challenging to perform in vitro and are extremely limited in vivo, especially inside the tissue volume. Here, we hybridized cells with silicon nanowires that transduced laser illumination into electrical interrogation in a simple, local, and leadless manner. We used these hybrids to address the question of whether cardiomyocytes and myofibroblasts electrically couple in vivo, which is important for understanding the contribution of scar tissue to abnormal electrical conduction in the heart. We found that although myofibroblasts were able to couple to cardiomyocytes in vitro, no such coupling was observed in vivo. This suggests that the degree of heterocellular electrical coupling in the whole heart is far less substantial than in cell culture.

Author contributions: M.Y.R. and B.T. designed research; M.Y.R., N.Y., and E.N.S. performed research; L.M., F.S., and B.T. contributed new reagents/analytic tools; M.Y.R., N.Y., E.N.S., and B.T. analyzed data; and M.Y.R. and B.T. wrote the paper.

The authors declare no competing interest.

This article is a PNAS Direct Submission.

Data deposition: The raw data that was used to generate Figs. 1–4 have been deposited on figshare (https://figshare.com/articles/Data_from_Living_myofibroblast_silicon_composites_for_probing_electrical_coupling_in_cardiac_systems/9968294).

[1]To whom correspondence may be addressed. Email: hrotenberg@uchicago.edu or btian@uchicago.edu.

This article contains supporting information online at www.pnas.org/lookup/suppl/doi:10.1073/pnas.1913651116/-/DCSupplemental.

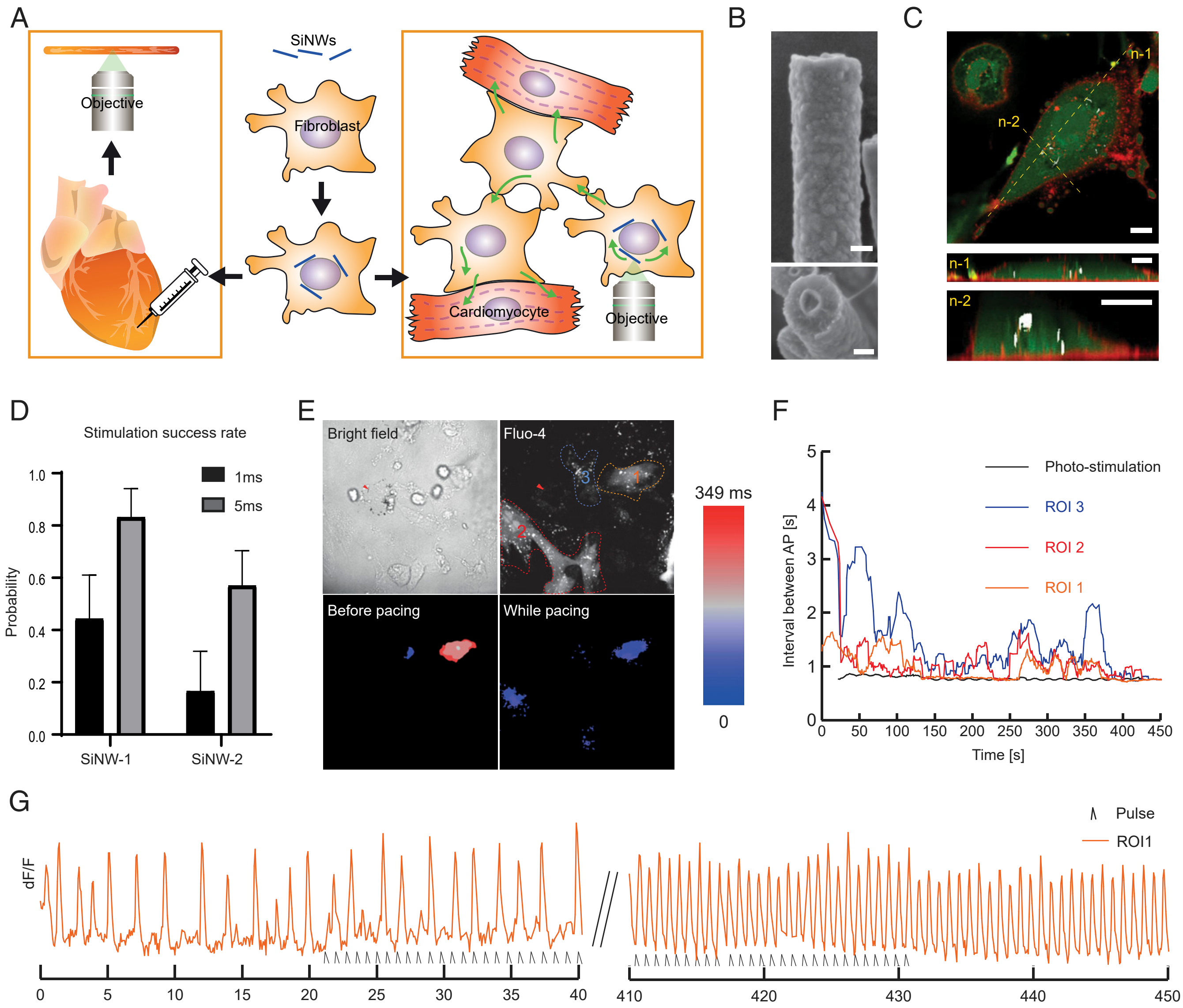

Fig. 1. In vitro electric coupling and optical pacing. (*A*) Illustration of the proposed MF–SiNW hybrid methodology. SiNWs are seeded on MFs and allowed to hybridize. The MF–SiNW hybrids can be harvested and cocultured with CMs or injected into heart tissue, where they provide high-resolution photomodulation. (*B*) SEM images of coaxial p-i-n SiNWs. (*Top*) One-dimensional morphology of an SiNW. (*Bottom*) Representative cross-section of a randomly broken SiNW, where the coaxial feature is clear. (Scale bars, 100 nm.) (*C*) Confocal images of cytoplasmatic (calcein AM, green) and membranal (CellMask, red) staining show that SiNWs are internalized by MFs. The SiNWs (white) are detected by reflected light. Yellow dashed lines represent 2 cross-sectioned z-n slices. (Scale bars, 10 μm.) (*D*) Longer pulse durations (1 ms or 5 ms, 1 mW) for SiNW stimulation increase the likelihood of provoking an AP in neighboring CMs. Results shown for 2 different SiNWs. Error bars represent SE of the mean from >20 stimulations for each SiNW. (*E*) Effect of photomodulation on MF–SiNW/CM coculture. (*Top Left*) Bright-field image shows perinuclear arrangement of SiNWs within MF; arrowhead indicates stimulated SiNW. (*Top Right*) Fluorescent Ca^{2+} imaging in analyzed ROIs 1 to 3. (*Bottom Left*) Heat map of AP propagation before photopacing shows unsynchronized CM beating in ROI 1 and 3, and no electrical activity in ROI 2. (*Bottom Right*) Following ∼400 s of photopacing (5 ms, 1 mW, 1.3 Hz), all regions are completely active and synchronized. Field of view: 169 μm × 169 μm. (*F*) Summary of activity in all ROIs following optical stimulation of MF–SiNW hybrid. Results are plotted as the average of the time intervals between consecutive APs for each ROI. Black line, pacing rate of laser pulse. (*G*) dF/F vs. time of electrical activity of ROI 1; initial slow rate of electrical activity gradually increases and synchronizes with the laser pulses.

morphology, as visible in a randomly broken SiNW (Fig. 1*B*). We then hybridized the free-standing SiNWs with primary MFs via spontaneous internalization (16) (Fig. 1*C*). We also verified MFs' viability by a live/dead assay, which showed negligible effect of the internalized SiNW on MFs' viability (*SI Appendix*, Fig. S1). To evaluate whether our MF–SiNW composites can enable electrical coupling in CMs in vitro, we optically stimulated a MF–SiNW hybrid cell in a coculture of CMs and MF–SiNWs and visualized the responses using the calcium-sensitive dye Fluo-4. In this setting, we applied a laser pulse focused at an SiNW within a MF–SiNW hybrid and monitored the effect of the photostimulation on neighboring CMs. The internalized SiNWs display random distributions of lengths, diameters, and locations. Therefore, it is difficult to determine a clear stimulation threshold. However, by applying laser stimulations of different durations (1 ms and 5 ms) on the same SiNWs, we determined that longer pulses were more likely to elicit an action potential (AP) in neighboring CMs (Fig. 1*D*). The threshold value of ∼5 μJ per pulse is comparable to that in the previously reported optical extracellular stimulation of neurons, where a 5.4-μJ threshold was identified (17). However, it is worth mentioning that we did not obtain the 1-to-1 AP per light pulse response, as was achieved for the neuromodulation (17). The intracellular location of the nanowires in the cells prevented us from further increasing the laser power without damaging the cell, while an extracellular configuration as used in the neuromodulation study (17) is more tolerant of light-triggered damage. Although it has been previously reported that MFs can mediate electrical activity between CMs in vitro (20–26), the ability of our MF–SiNW hybrid system to manipulate natural bioelectric signals in MFs and consequently modulate the electrical activity of neighboring CMs has not been reported.

We then asked if optical modulation of MF–SiNW hybrids could induce overdrive pacing in cocultured CMs. The bright-field contrast in Fig. 1 *E*, *Top Left* shows a perinuclear arrangement of SiNWs within an MF–SiNW hybrid, with the stimulated SiNW marked with a red arrow. Within this field, we selected 3 regions of interest (ROIs), each containing different CMs (Fig. 1 *E*, *Top Right*). Optical mapping of the calcium flux before stimulation showed that ROIs 1 and 3 were spontaneously active, but the timing of the contractions was not synchronized (Fig. 1 *E*, *Bottom Left* and Movie S1). As pacing requires repetitive stimulations, we lowered the laser power to ∼1 mW and paced the MF–SiNW hybrid at 1.3 Hz. Upon optical pacing, we observed a gradual increase in the ROI contraction rates. Fig. 1*F* plots the time intervals between consecutive contractions for each ROI; although immediate overdrive pacing was not observed, the contraction frequency gradually increased and approached the target pacing rate (1.3 Hz). Moreover, the optical stimulation also induced synchronization of the contractions in the different ROIs (Fig. 1 *E*, *Bottom Right* and Movie S1). As electrical coupling depends on the cell density and the location of the CMs relative to the stimulated MF–SiNW hybrid, the observed response to the stimulation differed among the ROIs. The contraction rate of ROIs 2 and 3, which were adjacent to the stimulated hybrid, immediately increased (Fig. 1*F*) upon stimulation. ROI 1, which was not in direct contact with the target hybrid, gradually synchronized to the target pacing rate (Fig. 1 *F* and *G*) with a slower response rate due to mediation of the signal by other cells (see *SI Appendix*, Fig. S2 for full dF/F trace). We also performed pacing with higher laser power, which resulted in an immediate, short-lived response, probably due to damage to the cells (*SI Appendix*, Fig. S3). Moreover, we showed that CMs can be paced to different frequency (∼0.75 Hz; *SI Appendix*, Fig. S4). These phenomena were observed in 5 independent cell cultures.

Investigation of In Vitro Heterocellular Electrical Coupling Using the MF–SiNW Hybrid

To demonstrate the utility of our hybrid tool to investigate in vitro intercellular electrical coupling, we optically stimulated an MF–SiNW hybrid in coculture and compared the resulting effect in neighboring MFs and CMs. Fig. 2*A* shows a coculture of cell–SiNW hybrids and CMs loaded with calcium-sensitive dye. Baseline recording of the cells revealed that 3 cells were spontaneously beating CMs, while the others were static MFs. Initially, the spontaneous AP propagation had a specific directionality (Fig. 2 *B*, *Left*). Upon optical stimulation, however, a local calcium flux was initiated at the stimulation site and all 3 neighboring CMs were immediately activated, with an AP propagating radially from the stimulated hybrid (Fig. 2 *B*, *Right*). Thereafter, a calcium flux slowly propagated through the MFs, as illustrated by mapping the long-term effect of the same optical stimulation (Fig. 2*C*, *SI Appendix*, Fig. S5, and Movie S2). Interestingly, the slow calcium flux through the MF–SiNWs seems to propagate entirely independently of the AP propagating through the CMs. This cell-specific response suggests that optical stimulation of the MF–SiNW activates 2 different mechanisms through which the calcium flux propagates through the coculture. We then used a pure MF culture, in which we stimulated different composites to better characterize the MF–MF coupling. Fig. 2*D* and Movie S3 show 2 representative results from the stimulation of 2 different MF–SiNW hybrids; the yellow arrows indicate the different directionality and signal propagations originating from the stimulated SiNWs. These results demonstrate our ability to control the origin of the stimulation with cell specificity and high spatial resolution using our cell–SiNW hybrid.

To quantify calcium propagation between and within different cell types, we used a computer algorithm (*Materials and Methods* and *SI Appendix*, Figs. S6–S8). Fig. 2*E* illustrates the propagation velocities 1) from the stimulated MF–SiNW hybrid to neighboring MFs (MF–MF), 2) within each MF (MF–intracellular), and 3) from the stimulated MF–SiNW hybrid to neighboring CMs (MF–CM). The fastest calcium propagation velocity (average 988 μm/s) was from MF–SiNW hybrids to CMs. This was significantly faster than propagation between MFs (MF–MF) and within each MF (MF–intracellular) ($P < 0.0001$ for both). This large difference in calcium propagation velocity rates supports our hypothesis that 2 different calcium flux propagation mechanisms exist in the coculture—one for the amplified CM propagation and the other for passive MF propagation. Moreover, a closer look at MF intracellular velocities revealed a decay in the differential of the flow with respect to the time of activation (Fig. 2*F*), meaning that MFs that are further down the propagation path demonstrate slower calcium flux propagation. We believe this calcium wave propagates freely through the cytosol to the borders of the MF; thereafter, it propagates to the neighbor MF through gap junctions (20, 21) or tunneling nanotubes (27), a bottleneck that slows down the propagation (Fig. 2*G*). This hypothesis explains 2 observed phenomena in our results on cultured MFs: The first is that the overall intercellular calcium wave propagation velocity, which combines the fast intracellular (MF–intracellular) and slow intercellular (MF–MF) propagation, is slower than the average intracellular MF calcium flux velocity (Fig. 2*E*), and the second is that the flow decays with time after the stimulation (Fig. 2*F*). To investigate whether the electrical coupling is mediated by gap junctions, we used carbenoxolone to completely block connexin 43. Indeed, upon stimulation of coculture with blocked gap junctions, only the stimulated cell was affected (*SI Appendix*, Fig. S9). We then showed that this effect was reversible, as changing the media to carbenoxolone free media showed that intercellular coupling was restored (*SI Appendix*, Fig. S9). We also performed immunocytochemistry staining for connexin 43 (*SI Appendix*, Fig. S10). The degree of connexin 43 expression between adjacent CMs was clearly higher than that between CMs and MFs, which was in turn higher than that between adjacent MFs. Overall, these results fit well with the accepted mechanism in which MFs passively mediate electrical coupling (20, 21).

In Vivo Seamless Integration of the MF–SiNW Hybrid

To use our hybrids to perform in vivo electrical interrogation with cell specificity and high spatial resolution, we first demonstrate that they can form a seamless integration with the contractile cardiac tissue. To show this, we injected either MF–SiNW hybrids or bare SiNWs into the left ventricular (LV) wall of a transplanted heart (Movie S4) to assess integration into cardiac tissue (Fig. 3*A*). Histological analysis, performed 2 to 5 d postprocedure, revealed hybrid MFs adjacent to healthy and striated native CMs (Fig. 3*B* and *SI Appendix*, Fig. S11). In hearts which had received bare SiNWs, we observed that the interface was encapsulated by fibrotic tissue that was significantly thicker than the tissue from the MF–SiNW-injected hearts (Fig. 3 *B* and *C* and *SI Appendix*, Fig. S11). In rare cases where bare SiNWs were near CMs, the CMs were visibly weakened, lacking striation. These bare SiNW-induced effects were accompanied by a dramatic increase in levels of the immune response-related proteins CD3 and CD11b (Fig. 3*E* and *SI Appendix*, Fig. S12), likely indicating direct irritation by the SiNWs and an inflammatory response. Hematoxylin and eosin staining (Fig. 3*D* and *SI Appendix*, Fig. S13) and Masson's trichrome stain (*SI Appendix*, Fig. S14) further validated the

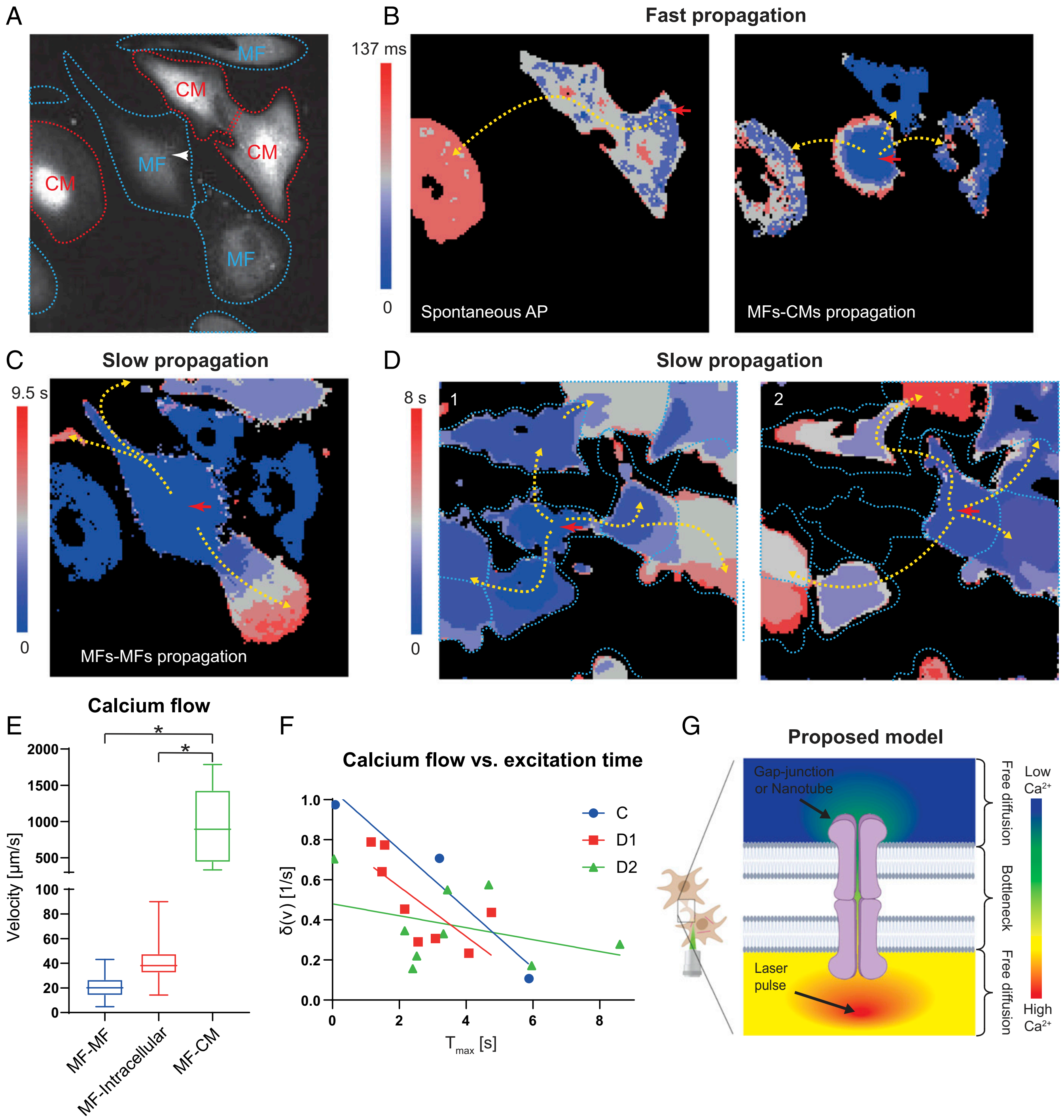

Fig. 2. Investigation of in vitro heterocellular electrical coupling using the MF–SiNW hybrid. (*A*) Fluorescent image of MF–SiNW hybrid (white arrowhead) and neighboring MFs (blue dashed lines) and CMs (red dashed lines) analyzed in *B* and *C*. Field of view: 169 µm × 169 µm. (*B*, *Left*) Heat map showing a spontaneous AP in CMs with specific directionality (yellow arrows). (*B*, *Right*) Heat map showing that optical stimulation of MF–SiNW hybrid results in a faster AP that propagates with different directionality to 3 adjacent CMs (yellow arrows). Field of view: 169 µm × 169 µm. (*C*) At a later time (9.5 s), a slow calcium flux (from the same optical stimulation) propagates through the MFs, independent of the optically induced APs in the CMs. Field of view: 169 µm × 169 µm. (*D*) Stimulation of 2 different MF–SiNW hybrids (red arrows) results in propagation of 2 different calcium waves. Field of view: 169 µm × 169 µm. (*E*) Calcium wave propagation from MFs to CMs (MF–CM) is significantly faster than propagation through neighboring MFs (MF–MF) or within MFs (MF–intracellular) ($*P < 0.0001$). Boxes represent quartiles, and whiskers represent minimum and maximum value ($n = 42$, 26, and 9 for MF–MF, MF–intracellular, and MF–CM, respectively). (*F*) MFs further down the propagation path demonstrate a decay in the calcium flux. (C, D1, and D2 correspond to C and D). (*G*) Proposed model for passive propagation within and between cells. Free passive diffusion is slowed by the bottleneck of intercellular gap junctions or tunneling nanotubes.

formation of thick fibrotic tissue by the bare SiNWs. Nuclear staining with a membrane-impermeable dye (propidium iodide; *SI Appendix*, Fig. S15) showed no difference in the number of dead cells between MF–SiNW hybrid hearts and bare SiNW hearts. The absence of dead cells in the bare SiNW hearts implies that any dead cells were likely removed and replaced by the fibrotic

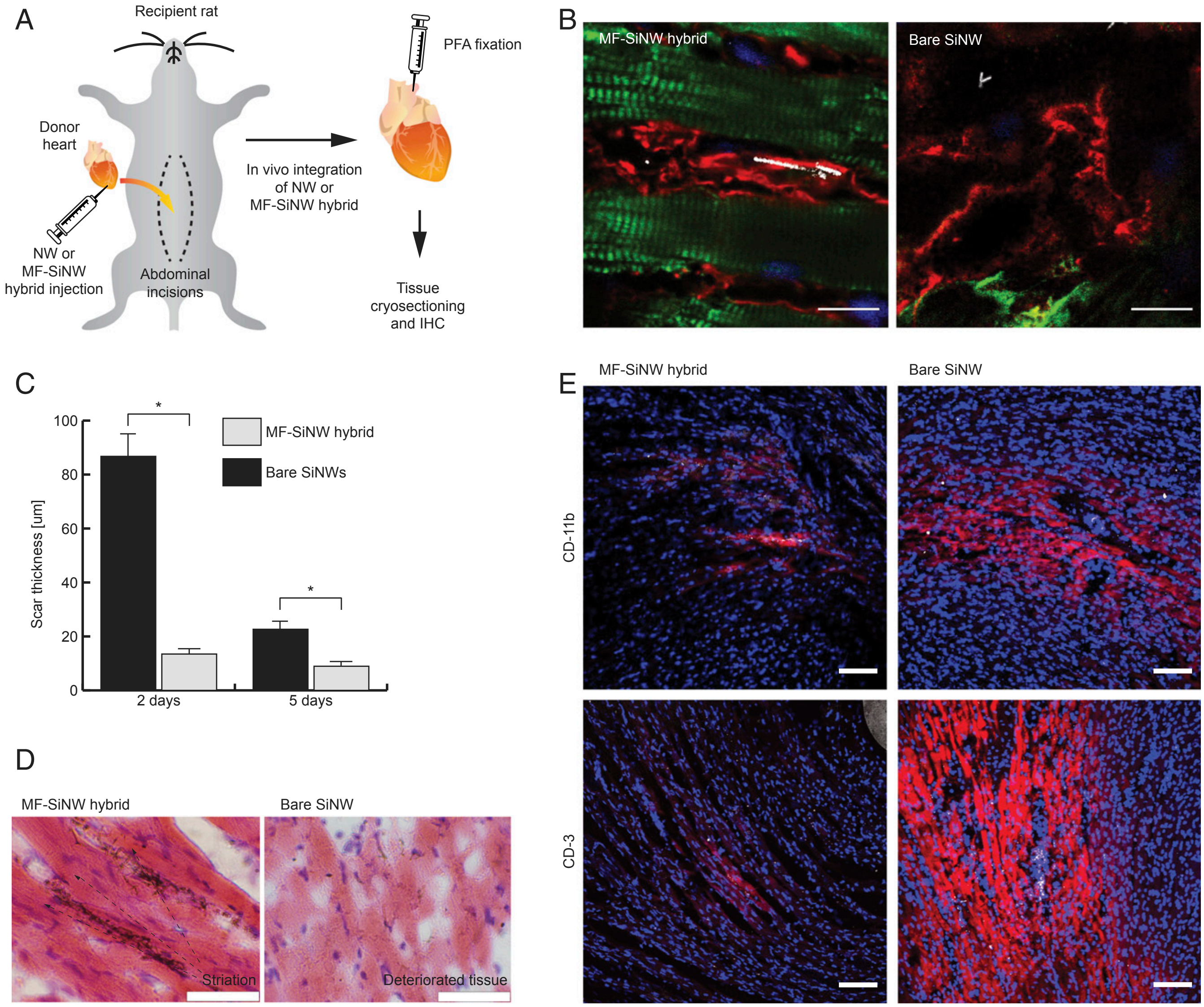

Fig. 3. In vivo seamless integration of the MF–SiNW hybrid. (*A*) Schematic of in vivo MF–SiNW experiment. Following transplantation, the donor heart is injected with MF–SiNW hybrids (5×10^4) or bare SiNWs (normalized to be half of total SiNW amount within hybrids). After 2 to 5 d, hearts are removed and fixed for immunohistochemistry (IHC). (*B*) IHC images of tissues injected with MF–SiNW hybrids or bare SiNWs. (*Left*) Hybrids are adjacent to native well-striated CMs (green); no fibrotic encapsulation is observed. (*Right*) Bare SiNWs (white) are encapsulated by fibrotic tissue and are not found near healthy CMs; closest CMs (green) lack striation and appear deteriorated. (Scale bars, 10 μm.) (*C*) Encapsulating scar thickness in hearts with MF–SiNW hybrids is significantly lower than in hearts with bare SiNWs ($*P < 0.001$). Two-day time point: $n = 9$ injections, $n = 3$ hearts; 5-d time point: $n = 6$ injections, $n = 2$ hearts). Error bars represent SE of the mean from $n > 20$ measurements. (*D*) Hematoxylin and eosin staining of the hybrids adjacent to well-striated CMs (*Left*) and bare SiNWs in the detreated tissue (*Right*). (Scale bars, 50 μm.) (*E*) IHC images of immune markers CD-11b and CD-3 show the low immune response to the hybrids as opposed to the bare SiNWs. (Scale bars, 100 μm.)

tissue over the 2 d following the transplant procedure. These observations indicate that the MF–SiNW hybrids are capable of seamlessly integrating in situ with cardiac tissue more effectively than bare SiNWs, supporting their use as a living bioelectric probe for studying MF–CM coupling.

Investigation of In Vivo Heterocellular Electrical Coupling Using the MF–SiNW Hybrid

In vitro electrical coupling between MFs and CMs is well established and has been extensively studied (20–26). However, the extent to which in vivo coupling between these 2 cell types occurs is still under debate and has only been studied indirectly (21, 28–33). We applied our MF–SiNW system, with its capacity for subcellular resolution, to this question. After the MF–SiNW hybrid integrated into the cardiac tissue, we harvested the heart to perform ex vivo investigation of the heterocellular coupling. Live tissue slices were cut with a vibratome (Fig. 4*A* and Movie S5), loaded with calcium-sensitive dye, and photostimulated via confocal microscopy. In this setting, the reflective nature of the SiNWs allowed us to easily detect the hybrid cells using transmitted light imaging (Fig. 4 *B*, *Top*) without genetic modifications. Optical mapping following laser stimulation (Fig. 4 *B*, *Bottom*) showed that the calcium flux propagated a short distance (<25 μm), affecting the stimulated cell and perhaps an adjacent cell. Although this does not entirely rule out the presence of gap junctions between the hybrids and native tissue, it does show that electrical coupling is far less substantial in vivo than in vitro. A contextual understanding of this result is important as theoretical models indicate that a substantial number of coupled MFs with a high degree of connectivity are required to induce significant arrhythmogenic effects (34, 35). Our findings seem to contradict recent studies which provided evidence that CM–MF coupling exists in vivo (29, 30). However, such coupling

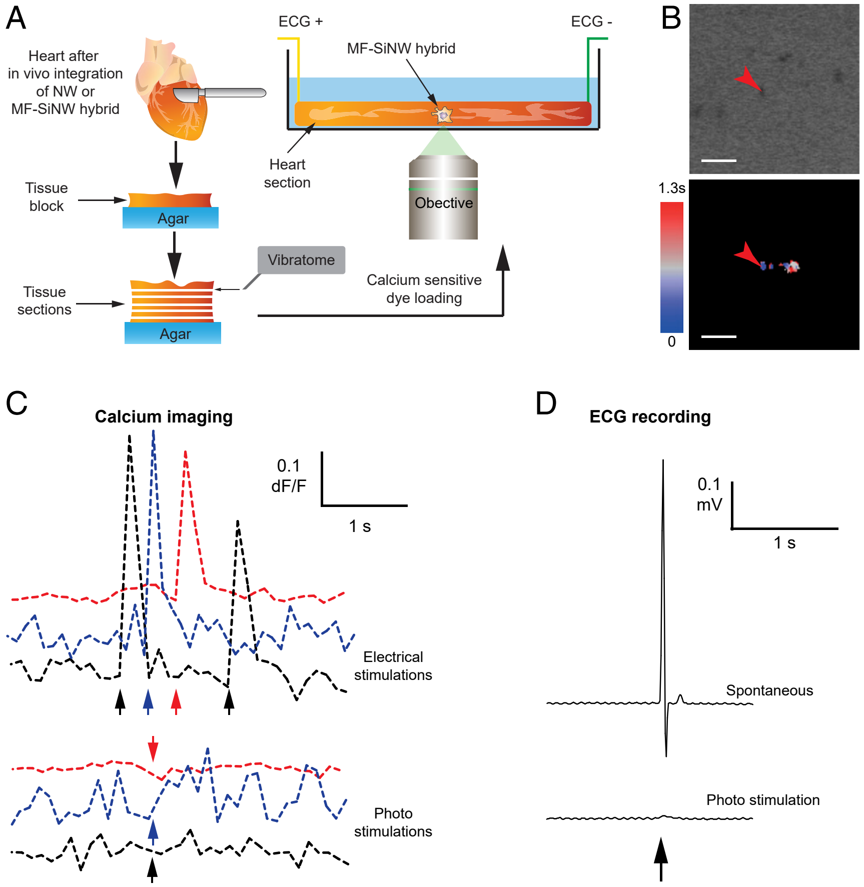

Fig. 4. Investigation of in vivo heterocellular electrical coupling using the MF–SiNW hybrid. (*A*) Schematic of the ex vivo MF–SiNW experiment. Following in vivo integration of the MF–SiNW hybrids, the removed hearts were sectioned into live tissue slices using vibrating microtome. Live heart slices are placed in a confocal microscope and SiNWs within hybrids are photostimulated. (*B*, *Top*) Transmitted light image of MF–SiNW hybrid and surrounding tissue showing location of laser stimulation. (*B*, *Bottom*) Optical mapping shows that the laser-induced calcium flux does not propagate to the tissue. (Scale bars, 20 μm.) (*C*) Calcium imaging of the heart slice. (*Top*) Tissue is healthy and responsive to standard electrical stimulation (positive control). (*Bottom*) Optical stimulation has no effect on the surrounding tissue. Colors represent separate photostimulations and corresponding electrical positive controls. (*D*) Upon laser illumination, no effect is recorded on ECG of the heart slice.

was evident only at the scar–myocardial border with no propagation into the scar (31). When we compare our observed in vivo photostimulation effect with our observed in vitro effect, and with reported in vitro effects from previous studies which showed that MFs relay signals up to distances of 300 μm (20), it is evident that direct coupling between MFs and other cells (MFs or CMs) is far less substantial in vivo. Even if the stimulated hybrid was not adjacent to native CMs, one would expect coupled MFs to propagate the effect to the interfaced tissue. To verify the tissue slice viability, we plotted the dF/F-vs.-time profile of nearby CMs. As a positive control, we recorded the effect of a standard electrical stimulation on the CMs immediately before applying the optical stimulation (Fig. 4 *C*, *Top*); a clear calcium flux resulted from electrical stimulation, confirming that the tissue was viable and electrically active. Immediately afterward, we recorded the effect of the laser pulse (Fig. 4 *C*, *Bottom*), which showed no response to the stimulation. Thus, the lack of response to optical stimulation may be attributed to weak coupling between MF–SiNW hybrids and the tissue. To further validate this, we also performed immunohistochemistry staining for connexin 43. Although this alone cannot rule out the existence of connexin 43 at MF–MF and MF–CM interfaces (28), the fact that the MF region (*SI Appendix*, Fig. S16) seems to lack connexin signal further supports our conclusion. Another important consideration is the cell integration duration that is needed for gap-junction formation in vivo. Although we have seen heterocellular electrical coupling in vitro occurring within 1 d of coculture, it is possible that in vivo coupling requires longer time. We tested integration duration of 2, 5, and 9 d posttransplantation, but there was no calcium propagation for tissue samples collected up to 9 d (*SI Appendix*, Fig. S17*B*).

Another aspect that needs to be considered is the fact that the native cardiac tissue functions as a syncytium of CMs (36, 37); the interconnected and large CMs result in extremely low input resistance and high capacitance. Therefore, the current threshold for sufficient depolarization is much higher in vivo than in vitro. However, this concern was addressed by previous work in which optogenetics was used for cardiac stimulation (38). Although higher levels of optical power density were used in vivo, they were comparable to that used in vitro (∼2:1 ratio). Therefore, in our in vivo study, we started with 4 mW of laser pulse. When no effect was obtained with 4 mW, we systematically increased the laser power up to 85 mW in vivo (vs. ∼4 to 7 mW in vitro, ∼20:1 ratio), which also did not yield any electrical response. To verify that the optical signal is not lost due to the relatively low temporal resolution of optical mapping, we also recorded an electrocardiograph (ECG) of the optically stimulated and spontaneously contracting tissue (Fig. 4*D*). Unlike the spontaneous APs recorded in the ECG (Fig. 4 *D*, *Top*), high-power laser pulses only resulted in a small artifact in the ECG (Fig. 4 *D*, *Bottom* and *SI Appendix*, Fig. S17*A*). This artifact was likely due to light diffraction from the tissue heating the electrodes. We also performed whole-heart experiments to establish the tissues' viability over a longer period (*SI Appendix*, Fig. S18). Despite the clear photoresponse shown as induced movement of SiNWs, no electrical effect was observed on the ECG recording (*SI Appendix*, Fig. S19). Taken together, our results suggest that while MF–CM coupling is observed in in vitro cultures it is significantly weaker in vivo.

Outlook

In summary, we have shown that hybridizing inorganic nanomaterials with cells allows for seamless integration with native tissue. The free-standing nature of our living, interconnect-free, and minimally invasive composite, along with silicon's ability to absorb tissue-penetrating near-infrared light, may give rise to future clinical applications. Our method allows precise cell-specific bioelectric induction with high spatial resolution and enables the optical identification of hybrids. It is simple, straightforward, and relies on standard optical microscopy with no need for sophisticated device fabrication or patch-clamp systems. We have demonstrated its utility in cardiac systems, as the contractile nature of the cardiac tissue poses a major challenge for establishing a seamless bioelectric interface from a mechanical prospective. However, our hybrid system may also be applied to many other biological scenarios where cell-specific interrogation and subsequent tracking of intercellular signal flow are required, such as the study of neuronal connectomics (39–41). One could also envision that the living cell–SiNW hybrid may be induced into a pluripotent stem cell, which can later be differentiated into many forms for nongenetic optical modulation.

Materials and Methods

Methods.

Nanowire synthesis. Coaxial p-i-n-SiNWs were synthesized using an Au nanocluster-catalyzed chemical vapor deposition (CVD) process. Au colloidal nanoparticles (100-nm diameter; Ted Pella) were deposited onto Si substrates (Nova Electronic Materials) for use as catalysts. During the SiNW growth, silane (SiH_4) was used as the Si reactant, diboron (B_2H_6, 100 ppm in H_2) as the p-type dopant, phosphine (PH_3, 1,000 ppm in H_2) as the n-type dopant, and hydrogen (H_2) as the carrier gas. For the p-type core SiNW growth, SiH_4, B_2H_6, and H_2 were delivered at flow rates of 2, 10, and 60 standard cubic centimeters per min (sccm), respectively. P-type core SiNW growth was carried out for 30 min at 470 °C and 40 torr. For the intrinsic Si shell (i-shell) deposition, the temperature was ramped up to 650 °C, during which time no gas flow was allowed, and vacuum was applied. Then, SiH_4 and H_2 were delivered at 0.3 and 60 sccm, respectively, at 15 torr. For the n-type outer shell, PH_3 gas was added at a flow rate of 1.5 sccm, under the same conditions. The shell depositions were performed at 750 °C at a pressure of 20 torr for 15 min per shell. Both intrinsic and n-type shells were grown for 20 min.

Cell culture. All animal procedures were approved by The University of Chicago Institutional Animal Care and Use Committee (IACUC) and conducted in complete compliance with the IACUC Animal Care and Use Protocol. Hearts were excised from postnatal day 0 to 5 neonatal rats into ice-cold Hanks' Balanced Salt Solution (HBSS) without Ca^{2+} or Mg^{2+}. Primary cardiac fibroblasts and CMs were isolated using the Pierce Primary Cardiomyocyte Isolation Kit (Thermo Fisher Scientific), according to the manufacturer's protocol. After isolation, the suspended cells were preplated for 1 to 2 h, allowing the fibroblasts to adhere to the tissue culture plate. The enriched CM population was seeded on fibronectin (Sigma)-treated glass bottom dishes. The fibroblasts were allowed to proliferate in culture media (DMEM high glucose + 10% FBS, 1% Glutamax and 1% penicillin–streptomycin) until cells reached ~80% confluency. As fibroblasts spontaneously differentiate into MFs in standard culture (42), we considered these cells to be MFs. The preplated MFs were then used for hybridization with SiNWs and coculture with CMs. For seeding SiNWs, 9 mm^2 of Si substrate with CVD-grown SiNWs was sonicated for 10 min in culture media and then seeded on MFs in a ~55-cm^2 dish (0.16-mm^2 chip per cm^2 culture). After 12 h, the culture was vigorously rinsed 5 to 8 times until no free-floating SiNWs were observed. Partially internalized SiNWs were allowed to complete internalization for 2 h. MF–SiNW hybrids were harvested via trypsinization for 2 min and then rinsed and centrifuged for 5 min at 200 × *g* (low *g* was used to avoid damage to the cells due to mechanical stress and strain by the SiNWs). Harvested MF–SiNW hybrid cells were reseeded alone, cocultured with CMs, or injected into hearts.

Live/dead assay. Cells were treated with different concentrations of SiNWs for 12 h. Then, SiNWs were rinsed away and cells were loaded with LIVE/DEAD Viability/Cytotoxicity Kit, for mammalian cells (Thermo Fisher Scientific), which consists of calcein AM (4 μM) and ethidium homodimer-1 (2 μM) for 30 min. Cell were imaged immediately after rinsing the dye off.

In vitro optical stimulation. Cells (MFs or MFs–CMs coculture) were treated with calcium-sensitive dye (2 μM Fluo-4, AM, cell permeant; Thermo Fisher Scientific) for 30 min at 37 °C. Cells were rinsed and incubated for 30 min to allow complete deesterification. The treated cells were then analyzed using a Marianas Yokogawa-type spinning disk confocal for visualizing and stimulating the cells. The Marianas Yokogawa confocal system allows setting a stimulation point for a designated time in-between recorded time frame. However, the time duration for switching the optical shutter from recording to stimulation varied. Consequently, the resulting pacing rate had an SD of ~6%. Thus, Fig. 1*F* shows the moving average of the pacing rate throughout the experiment. For blocking connexin 43, we treated the cells with 500 μM carbenoxolone (Apexbio) in DMEM for 30 min. After stimulation, the media was replaced with fresh carbenoxolone free media to reverse the blocking effect.

Immunocytochemistry. Cells (MFs or MFs–CMs coculture) were fixed (4% paraformaldehyde; Sigma) and permeabilized (0.2% Triton X-100; Sigma). The cells were blocked (2% bovine serum albumin) to prevent nonspecific binding and incubated with rabbit anti-cardiac troponin I antibody (Abcam; for CMs), chicken anti-Vimentin antibody (Abcam; for MFs), and mouse anti-Connexin 43 antibody (Abcam). Cells were then incubated with Alexa Fluor 488, Alexa Fluor 647, and Alexa Fluor 568 secondary antibodies (Abcam). ProLong Gold Antifade Mountant with DAPI (Themo Fisher) was used to label the nuclei and the cells were imaged using the Leica SP5 Tandem Scanner Spectral 2-Photon Confocal.

Optical mapping. Fluo-4 videos were analyzed using ImageJ (43) and an online available macro (44) for creating ΔF/F movies. The videos were made into binary masks according to a threshold manually selected as activated/not activated, and the resulting stack was used to generate a time color code for the activation propagation.

We measured the intracellular speed of calcium signals by tracking the wave front in each cell using a thresholded kymograph along the axis of propagation (*SI Appendix*, Fig. S6). At each time point, the position of the signal front is given by the boundary between the thresholded and nonthresholded regions. To calculate the average speed of the signal along the length of the kymograph, we fit a line by eye to the boundary, such that the slope of the line equals the speed.

To quantify the rate of intercellular propagation, we analyzed the optical flow of ΔF/F movies. The optical flow was estimated with the Lucas–Kanade method as implemented in the MATLAB Image Processing Toolbox (The MathWorks). To identify the time of calcium activation in cells, we considered that the mean optical flow, $<\nu>$(t), of a region enclosed by the boundaries of the cell is initially very low, undergoes a rapid increase alongside the fluo-4 signal upon activation, and then gradually decays in the absence of any further stimulation (*SI Appendix*, Fig. S7, *Top*). For ease of visualization, the $<\nu>$ signal is normalized to the initial time point for each cell. We can then characterize the activation time of a cell as the point where the differential of the mean optical flow signal reaches its peak (*SI Appendix*, Fig. S7, *Bottom*) We smoothed the mean optical flow signal using a Gaussian filter with $\sigma = 3\Delta t$, where Δt is the time interval between frames in the movie, and found the maximum of the function $\Delta\langle\nu\rangle(t) = \nu(t+3\Delta t) - \langle\nu\rangle(t-3\Delta t)$ as the differential, an analogy to the derivative. We adopted this latter step in order to account for the variation different cells showed in the time to reach the maximum mean flow (Fig. 2*F* and *SI Appendix*, Fig. S8). Finally, we calculated the speed of the calcium signal between cells *i* and *j* as $v_{Ca^{2+}} = (t_{max,j} - t_{max,i})/r_{ij}$, where r_{ij} is the distance between the centroid of the 2 cells.

In vivo hybrid integration. All animal procedures were approved by The University of Chicago IACUC and conducted in complete compliance with the IACUC Animal Care and Use Protocol. For cardiac transplantation, we used 2 rats (donor and recipient) per surgery. Following anesthetic induction and stabilization, the donor animal's chest and the recipient animal's abdominal areas were shaved and aseptically prepared. For donor surgery, the chest was opened and the heart exposed. After isolation and ligation of the superior/inferior vena cava and pulmonary vein, the aorta and pulmonary artery were cut and the heart was collected. The heart was preserved in cold saline awaiting transplantation. For recipient surgery, the animal's abdominal cavity was opened, and the aorta and vena cava were isolated and exposed. Using 10-0 nylon sutures, the donor's aorta was connected to the recipient's aorta and the donor's pulmonary artery was connected to the recipient's inferior vena cava. Upon the completion of transplantation, the muscle and chest peritoneum inner layers were sutured with 5-0 monofilament sutures. Subcutaneous tissue and skin were sutured with 5-0 monofilament nonabsorbable sutures. Immediately after blood flow to the transplanted heart was resumed, we injected the hybrids (5×10^4 cells) or bare SiNWs (normalized to be half of the total amount of SiNWs within the MF–SiNW hybrids, discussed below) into 3 different locations in the LV wall. After the procedure, the rats were treated daily with cyclosporin A (15 mg/kg) and methylprednisolone (2 mg/kg) to prevent immune rejection. After the designated time (2 to 9 d), the heart was excised from the recipient abdomen and used for ex vivo Langendorff perfused heart model ($n = 4$ for bare NWs and $n = 6$ for MF–SiNW hybrids) or sectioned to live tissue slices ($n = 4$ for bare NWs and $n = 5$ for MF–SiNW hybrids). Immunohistochemistry was performed on the unstimulated parts of the injection site.

To measure the amount of SiNWs that were internalized by the MFs, we drop-casted 50 μL of SiNWs suspension before seeding on the cells. Thereafter, to avoid coffee ring formations while drying, we mounted a coverslip and imaged the suspension immediately using dark-field microscopy (*SI Appendix*, Fig. S20). Then, after the SiNWs were internalized, we collected a sample of the media with noninternalized SiNWs and repeated the procedure. We then calculated the number of pixels that were positive for SiNWs (all frames were given the same threshold), which correlated to the amount of NWs in the suspension. The difference in SiNW-occupied area between the samples before and after introduction to cells trends roughly proportional to the amount of internalized SiNWs. From this procedure, we found that approximately half of SiNWs were internalized; as such, we used half of the amount of NWs that were internalized as the control of bare SiNWs injected in vivo.

Immunohistochemistry. Hearts were excised from the recipient rat's abdomen. The LV wall was removed and embedded in optimal cutting temperature compound (Fisher Scientific). Samples were snap-frozen in isopentane using dry ice and stored at –80 °C. The frozen tissue was cut into 10-μm slices using a cryotome (Cryostat NX50). The tissue sections were processed for standard immunohistochemistry (same antibodies as for in vitro cells, plus antibodies against immune response proteins CD3 and CD11b). Other slices were processed for standard hematoxylin and eosin or Masson's trichrome staining.

Vibratome sectioning of live tissue slices. Following removal from the recipient rat's abdomen, the heart was placed in ice-cold HBSS buffer, and the aorta was cannulated in preparation for use in a Langendorff setup. Oxygenated Hepes-buffered Tyrode's solution (containing 126 mM NaCl, 5.4 mM KCl, 10 mM glucose, 10 mM Hepes, 1 mM $MgCl_2$, 2 mM $CaCl_2$, 1.2 mM $MgSO_4$, and 0.39 mM NaH_2PO_4; bubbled with 99.5% O_2; pH 7.3) was perfused through the cannulated aorta. The perfusion was passed through a heating coil and bubble trap (Radnoti), and the heart was placed in a water-jacketed beaker (Fisher Scientific) to maintain the temperature at 37 °C. Rhod-2 calcium dye (5 μM; Abcam), and Pluronic F-127 (Thermo Fisher Scientific) were added to the perfusion buffer and loaded into the hearts (45). After 20 min of dye loading, the heart was perfused with dye-free media for 30 min and moved to ice-cold oxygenated buffer. The heart was cut into live tissue slices according to Watson et al. (46). Briefly, the LV was removed and glued (Medbond Tissue Glue; Stoelting Co.) to an agar substrate so that the muscle fibers would be aligned to the blade. A sapphire blade was used on a Leica VT1000 S vibratome to slice the heart while immersed in ice-cold oxygenated buffer, and the slices were kept in the same cutting buffer for up to 3 h.

Ex vivo optical stimulation of tissue slices. Slices of the heart were moved to a prewarmed microscope stage and allowed to equilibrate to 37 °C for 20 to 30 min while bubbled with oxygen. A Leica SP5, STED-CW Superresolution Laser Scanning Confocal was used to visualize the MF–SiNW hybrids within the tissue, and the STED setting was used to apply high-power optical stimulation. The stimulated slices were visualized to record calcium flux changes as a result of optical stimulation. An SI-200 Stimulus Isolator (IWorx) was used to apply electrical stimulation as a positive control to verify slice viability. To perform the ECG recording of optical stimulation and spontaneous contractions (not of electrical stimulation), we used an isolated Biopotential recording preamplifier (C-ISO-256; IWorx) and an amplifier (IA-400D; IWorx) that were connected to a digitizer (DI-1100; DataQ).

Statistical analysis. We used GraphPad Prism 8 to perform all statistical analysis. For propagation velocities we used 1-way ANOVA with Tukey's multiple comparisons test. For scar size we used unpaired t test. In all datasets, $P < 0.05$ was considered significant.

Data availability. The raw data that was used to generate Figs. 1 *B*–*G*, 2 *A*–*F*, 3 *B*–*E*, and 4 *B*–*D* have been deposited on figshare (47). These data include: raw SEM images (Fig. 1*B*); z-stack of confocal imaging (Fig. 1*C*); raw videos of the photostimulations (sld files, Fig. 1*D*); raw video of the photostimulation, bright filed image of the SiNWs, fluorescent image of the fluo-4, and a text file with the stimulation timings (Fig. 1 *E*–*G*); raw video of the photo-stimulation (Fig. 2 *A*–*C*); raw videos of the photostimulations (*D1*, *D2*, *i*, *ii*, *iii*, *iv*, *v*, and *vi*) (Fig. 2 *D*–*F*); z-stack of confocal imaging of the scar (Fig. 3*B*); images of the scar with the scar thickness as used for statistical analysis (Fig. 3*C*); Hematoxylin and Eosin images of the scar (Fig. 3*D*); z-stack of confocal imaging of the scar immune response (Fig. 3*E*); raw video of the photostimulation and the transmitted light image showing the SiNWs (Fig. 4*B*); raw videos of the 3 different photostimulations and their intensity profiles (Fig. 4*C*); and ECG recording of the optical and electrical stimulation (Fig. 4*D*).

ACKNOWLEDGMENTS. We thank Karen Watters for scientific editing of the manuscript; Prof. Yoram Etzion from Ben-Gurion University of the Negev and Prof. Ilya A. Fleidervish from Ben-Gurion University of the Negev for their scientific consultation and brainstorming; Prof. Margaret Gardel from The University of Chicago for her technical assistance; and the Human Tissue Resource Center at The University of Chicago, the Integrated Light microscopy Core Facility at The University of Chicago, and the Animal Microsurgery Center (CORE) at The University of Chicago for their technical assistance. This work is supported by the Air Force Office of Scientific Research (AFOSR FA9550-18-1-0503), US Army Research Office (W911NF-18-1-0042), US Office of Naval Research (N000141612530, N000141612958), and the National Institutes of Health (NIH NS101488)

1. B. Sakmann, E. Neher, Patch clamp techniques for studying ionic channels in excitable membranes. *Annu. Rev. Physiol.* **46**, 455–472 (1984).
2. K. Jayant *et al*., Targeted intracellular voltage recordings from dendritic spines using quantum-dot-coated nanopipettes. *Nat. Nanotechnol.* **12**, 335–342 (2017).
3. C. Xie, Z. Lin, L. Hanson, Y. Cui, B. Cui, Intracellular recording of action potentials by nanopillar electroporation. *Nat. Nanotechnol.* **7**, 185–190 (2012).
4. J. T. Robinson *et al*., Vertical nanowire electrode arrays as a scalable platform for intracellular interfacing to neuronal circuits. *Nat. Nanotechnol.* **7**, 180–184 (2012).
5. X. Duan *et al*., Intracellular recordings of action potentials by an extracellular nanoscale field-effect transistor. *Nat. Nanotechnol.* **7**, 174–179 (2011).
6. B. Tian *et al*., Three-dimensional, flexible nanoscale field-effect transistors as localized bioprobes. *Science* **329**, 830–834 (2010).
7. Q. Qing *et al*., Free-standing kinked nanowire transistor probes for targeted intracellular recording in three dimensions. *Nat. Nanotechnol.* **9**, 142–147 (2014).
8. A. M. Packer, B. Roska, M. Häusser, Targeting neurons and photons for optogenetics. *Nat. Neurosci.* **16**, 805–815 (2013).
9. E. S. Boyden, F. Zhang, E. Bamberg, G. Nagel, K. Deisseroth, Millisecond-timescale, genetically targeted optical control of neural activity. *Nat. Neurosci.* **8**, 1263–1268 (2005).
10. A. M. Packer, L. E. Russell, H. W. Dalgleish, M. Häusser, Simultaneous all-optical manipulation and recording of neural circuit activity with cellular resolution in vivo. *Nat. Methods* **12**, 140–146 (2015).
11. B. Tian, C. M. Lieber, Synthetic nanoelectronic probes for biological cells and tissues. *Annu. Rev. Anal. Chem. (Palo Alto, Calif.)* **6**, 31–51 (2013).
12. D. H. Kim, R. Ghaffari, N. Lu, J. A. Rogers, Flexible and stretchable electronics for biointegrated devices. *Annu. Rev. Biomed. Eng.* **14**, 113–128 (2012).
13. K. J. Yu, Z. Yan, M. Han, J. A. Rogers, Inorganic semiconducting materials for flexible and stretchable electronics. *NPJ Flexible Electronics* **1**, 4 (2017).
14. S. P. Lee *et al*., Highly flexible, wearable, and disposable cardiac biosensors for remote and ambulatory monitoring. *NPJ Digit Med* **1**, 2 (2018).
15. G. Hong, C. M. Lieber, Novel electrode technologies for neural recordings. *Nat. Rev. Neurosci.* **20**, 330–345 (2019).
16. J. F. Zimmerman *et al*., Cellular uptake and dynamics of unlabeled freestanding silicon nanowires. *Sci. Adv.* **2**, e1601039 (2016).
17. R. Parameswaran *et al*., Photoelectrochemical modulation of neuronal activity with free-standing coaxial silicon nanowires. *Nat. Nanotechnol.* **13**, 260–266 (2018).
18. Y. Jiang *et al*., Rational design of silicon structures for optically controlled multiscale biointerfaces. *Nat. Biomed. Eng.* **2**, 508–521 (2018).
19. B. Tian *et al*., Coaxial silicon nanowires as solar cells and nanoelectronic power sources. *Nature* **449**, 885–889 (2007).
20. G. Gaudesius, M. Miragoli, S. P. Thomas, S. Rohr, Coupling of cardiac electrical activity over extended distances by fibroblasts of cardiac origin. *Circ. Res.* **93**, 421–428 (2003).
21. A. Klesen *et al*., Cardiac fibroblasts : Active players in (atrial) electrophysiology? *Herzschrittmacherther. Elektrophysiol.* **29**, 62–69 (2018).
22. K. Goshima, Synchronized beating of and electrotonic transmission between myocardial cells mediated by heterotypic strain cells in monolayer culture. *Exp. Cell Res.* **58**, 420–426 (1969).
23. A. Hyde *et al*., Homo-and heterocellular junctions in cell cultures: An electrophysiological and morphological study. *Prog. Brain Res.* **31**, 283–311.
24. K. Goshima, Formation of nexuses and electrotonic transmission between myocardial and FL cells in monolayer culture. *Exp. Cell Res.* **63**, 124–130 (1970).
25. P. Kohl, A. G. Kamkin, I. S. Kiseleva, D. Noble, Mechanosensitive fibroblasts in the sino-atrial node region of rat heart: Interaction with cardiomyocytes and possible role. *Exp. Physiol.* **79**, 943–956 (1994).
26. P. Camelliti, C. R. Green, P. Kohl, "Structural and functional coupling of cardiac myocytes and fibroblasts" in *Cardiovascular Gap Junctions*, S. Dhein, Ed. (Karger Publishers, 2006), vol. 42, pp. 132–149.
27. K. He *et al*., Long-distance intercellular connectivity between cardiomyocytes and cardiofibroblasts mediated by membrane nanotubes. *Cardiovasc. Res.* **92**, 39–47 (2011).

28. P. Kohl, R. G. Gourdie, Fibroblast-myocyte electrotonic coupling: Does it occur in native cardiac tissue? *J. Mol. Cell. Cardiol.* **70**, 37–46 (2014).
29. T. A. Quinn *et al*., Electrotonic coupling of excitable and nonexcitable cells in the heart revealed by optogenetics. *Proc. Natl. Acad. Sci. U.S.A.* **113**, 14852–14857 (2016).
30. M. Rubart *et al*., Electrical coupling between ventricular myocytes and myofibroblasts in the infarcted mouse heart. *Cardiovasc. Res.* **114**, 389–400 (2018).
31. S. Nattel, Electrical coupling between cardiomyocytes and fibroblasts: Experimental testing of a challenging and important concept. *Cardiovasc. Res.* **114**, 349–352 (2018).
32. A. M. De Mazière, A. C. van Ginneken, R. Wilders, H. J. Jongsma, L. N. Bouman, Spatial and functional relationship between myocytes and fibroblasts in the rabbit sinoatrial node. *J. Mol. Cell. Cardiol.* **24**, 567–578 (1992).
33. P. J. Lafontant *et al*., Cardiac myocyte diversity and a fibroblast network in the junctional region of the zebrafish heart revealed by transmission and serial block-face scanning electron microscopy. *PLoS One* **8**, e72388 (2013).
34. S. Rohr, Arrhythmogenic implications of fibroblast-myocyte interactions. *Circ Arrhythm Electrophysiol* **5**, 442–452 (2012).
35. K. A. MacCannell *et al*., A mathematical model of electrotonic interactions between ventricular myocytes and fibroblasts. *Biophys. J.* **92**, 4121–4132 (2007).
36. S. Weidmann, The diffusion of radiopotassium across intercalated disks of mammalian cardiac muscle. *J. Physiol.* **187**, 323–342 (1966).
37. W. C. De Mello, Effect of intracellular injection of calcium and strontium on cell communication in heart. *J. Physiol.* **250**, 231–245 (1975).
38. T. Bruegmann *et al*., Optogenetic control of heart muscle in vitro and in vivo. *Nat. Methods* **7**, 897–900 (2010).
39. A. Fornito, A. Zalesky, M. Breakspear, The connectomics of brain disorders. *Nat. Rev. Neurosci.* **16**, 159–172 (2015).
40. H. Zeng, J. R. Sanes, Neuronal cell-type classification: Challenges, opportunities and the path forward. *Nat. Rev. Neurosci.* **18**, 530–546 (2017).
41. J. W. Lichtman, J. Livet, J. R. Sanes, A technicolour approach to the connectome. *Nat. Rev. Neurosci.* **9**, 417–422 (2008).
42. S. Rohr, Cardiac fibroblasts in cell culture systems: Myofibroblasts all along? *J. Cardiovasc. Pharmacol.* **57**, 389–399 (2011).
43. C. T. Rueden *et al*., ImageJ2: ImageJ for the next generation of scientific image data. *BMC Bioinformatics* **18**, 529 (2017).
44. J. Ackman, dFoFmovie-CatFullAutoSave.java. https://gist.github.com/ackman678/11155761. Accessed 9 October 2019.
45. K. Wang *et al*., Cardiac tissue slices: Preparation, handling, and successful optical mapping. *Am. J. Physiol. Heart Circ. Physiol.* **308**, H1112–H1125 (2015).
46. S. A. Watson *et al*., Preparation of viable adult ventricular myocardial slices from large and small mammals. *Nat. Protoc.* **12**, 2623–2639 (2017).
47. M. Y. Rotenberg, Data from: Living myofibroblast–silicon composites for probing electrical coupling in cardiac systems. figshare. https://figshare.com/articles/Data_from_Living_myofibroblast_silicon_composites_for_probing_electrical_coupling_in_cardiac_systems/9968294. Deposited 10 October 2019.